Microstructure Evolution in AM Produced Superalloy Thin Struts at Low Plastic Strain

Laura Delcuse, Slim Bahi, U.F. Gunputh, M. Ben Haj Slama, Antoine Guitton, Alexis Rusinek, Nabila Maloufi, G. Williams, P. Wood

Microstructure Evolution in AM Produced Superalloy Thin Struts at Low Plastic Strain

L. DELCUSE[a], S. BAHI[a], U.F. GUNPUTH[b], M. BEN HAJ SLAMA[a], A. GUITTON[a], A. RUSINEK[a, c], N. MALOUFI[a], G. WILLIAMS[b], P. WOOD[b]

Corresponding Author: mohamed-slim.bahi@univ-lorraine.fr
[a] Université de Lorraine -- CNRS -- Arts et Métiers -- LEM3, 57070 Metz, France
[b] College of Science and Engineering, University of Derby, Quaker Way, Derby, United Kingdom
[c] Chair of Excellence, Department of Mechanical Engineering, University Carlos III of Madrid, Avda. Universidad 30, 28911 Leganés, Madrid, Spain

ABSTRACT
This paper discusses the microstructures and textures that develop in thin struts fabricated in Inconel 718 using laser melting powder bed fusion. Thin struts 1 mm wide were fabricated in the vertical (ZX) and horizontal build (XY) orientations with respect to the build plate. Three distinct regions of well-defined grain structures with centerline symmetry from the outer border to the center of the inner volume were present, which was attributed to the laser scan strategy, consisting of a fill hatch, inner and outer border scan on each 30 □m layer. Using ex situ micro-tensile testing and enhanced Back-Scattered Electrons (BSE) and Electron Back Scattered Diffraction (EBSD), the microstructure evolution to a plastic strain near 1%, in both the ZX and XY build direction was studied in the initial undeformed and final deformed states. For the ZX build direction, grain rotation as well as grain boundary migration was observed and was more significant than in the samples fabricated in XY. This paper discusses the evolution of the microstructure offering valuable insights into the relationship between microstructure and mechanical properties in complex AM produced microstructures.

Keyword: Inconel 718, Additive manufacturing, Complex microstructures, Border and volume fill scan, Thin struts, Microscale testing

1.0 INTRODUCTION
Nickel-based superalloys, known for their high strength, excellent creep properties, and good corrosion resistance [1-3], are extensively used in various industrial applications such as gas turbines and aerospace. Among these superalloys, Inconel 718 is a Ni-Fe-Cr alloys, with a face centered cubic (FCC) NiCr phase γ as major phase [4-7]. The γ matrix is strengthened by a body-centered tetragonal (DO22) crystal structure [8-10] γ" (Ni3Nb) phase and by a cubic ordered face centered (Ll2) γ’ (Ni3Al) phase [4, 5, 8-13]. The phase γ’’ is a metastable phase which can transform into an orthorhombic (DOa) δ-phase (Ni3Nb) [4]. This phase precipitates mainly at grain boundaries and presents an enrichment in Nb [2, 10-12, 14]. The δ-phase morphology consists in plate needles arranged in a parallel way [7, 8, 15]. While the presence of the δ-phase can enhance the alloy's strength, it can also reduce its ductility [8, 16]. A low amount of the δ-phase can be beneficial in improving creep resistance by impeding crack propagation [17]. Heat treatment can be employed to control the formation and fraction of the δ-phase [4, 18]. Another intermetallic phase in Inconel 718 is Laves phase, which forms in the interdentritic region [2, 12] and exhibits a significant Nb. The Laves phase has a globular shape and contained approximately 25% weight of Nb [12, 13, 19]. The precipitation of Laves phase occurs within a temperature range of 650 °C to 1100 °C [10]. The amount of Laves phase decreases with increasing cooling rate, as observed during the manufacturing and post-treatment processes [4, 11]. Considering the decrease of the principal alloying element (Ni) in the matrix and the increase of the amount of Nb, the presence of Laves phase imparts a brittle nature to the material [12, 13, 16, 19] . Additionally, the bonding between the Laves phase and the matrix is weak, resulting in debonding under relatively lower stress. The quantity of Laves phase can be controlled through homogenization heat treatment, which partially dissolves the Laves phase at high temperatures [6, 11, 13].

Understanding the complex deformation mechanisms and the evolution of microstructure during manufacturing processes is a major challenge in studying Inconel 718, given the presence of multiple phases. In this paper, the manufacturing process employed for Inconel 718 is Laser-based Powder Bed Fusion (L-PBF), also known as Selective Laser Melting (SLM). This layer-by-layer additive manufacturing process offers novelty in terms of mechanical properties [14] and lattice structure [20, 21]. The presence of porosities, the microstructure organization, and the relative density in L-PBF-manufactured parts depend on various process parameters, such as laser power [22-25], scan strategy [24, 26-28], scanning speed of the laser [29, 30] and volumetric energy density (VED) [31] . Moreover, the building direction has also a significant influence on the microstructure, since it determines the grains orientation as well as their size [4, 5, 32, 33]. Several studies have demonstrated the effect of this variation in the obtained microstructure on the mechanical properties [34-37]. The laser scanning strategy during the LPBF process has also been shown to be key in determining the surface roughness, density, microstructure and mechanical properties of AM parts [38]. Examples of different scanning strategies are unidirectional, island, helix, contour, cross scan and meander scanning. Jia et al. [38] concluded that rotating alternate layers during a LPBF process, reduces texture and anisotropy of AM parts. Tian et al. [39] further concluded that contour scanning strategy reduces surface roughness while increasing the density of LPBF parts.

Microstructure analysis plays a crucial role in understanding the mechanical properties, particularly in additive manufacturing (AM) processes, which result in complex microstructures due to non-equilibrium phenomena (solidification, rapid cooling, etc..). Previous studies have reported the existence of complex microstructure near the edges of L-PBF-built samples [40] [41]. However, the evolution of these edge microstructure, as well as the microstructure in the rest of the samples, has not been investigated under deformation loading. In this study, micro-tensile tests coupled with Scanning Electron Microscope (SEM) were performed to examine the relationship between different additive manufacturing processes and the associated microstructure, with a focus on comparing edge microstructures [42]. Micro-tensile testing using an SEM has commonly been used to investigate the evolution of microstructure under uniaxial loading [43-45]. Recently, enhanced backscattered-electron images (BSE) have been employed to characterize deformation structures, such as slip lines and dislocations, during macro-mechanical testing of polycrystalline bulk titanium alloy specimens inside SEM [43, 46].

Manufacturing thin struts using LPBF process is different from manufacturing bigger bulk samples [42]. There is a unique heat and mass transfer phenomenon followed by a unique external stress in a small contact area during the LPBF process. Inconel 718 manufactured by an LPBF process have fine grains and as such manufacturing thin walled IN718 parts require more understanding of the printing parameters and the resulting microstructure. Yang et al. [42] observed significant differences in the edge microstructure of 0.2 mm thick struts as compared to the mid-section of the latter which further affected its mechanical properties. Further work is needed to understand the effect of loading on similar struts with different border microstructures.

The main objective of this work is to characterize the microstructure of additively manufactured Inconel 718 thin struts obtained in the vertical (ZX) and horizontal (XY) respect to the building directions using L-PBF. Ex-situ micro-tensile tests was conducted with plastic deformation going just beyond yield approaching 1% tensile plastic strain to study the deformation of the complex microstructure. The grain structures, and second phases were analyzed using enhanced BSE and Electron Back Scattered Diffraction (EBSD) measurements before and after micro-tensile loading. The influence of the building direction on the initial and final microstructures together with the effect on plastic deformation at low plastic strain is discussed.

2.0 MATERIALS AND METHODS

2.1 Laser Powder Bed Fusion process

The Laser-based Powder Bed Fusion (L-PBF) process consists of spreading a layer of powder by a blade on a substrate plate. The powder layer is then melted using a laser under an inert gas atmosphere, such as Argon. This process is repeated layer by layer until the final product is fabricated. In this study, a Renishaw AM250 machine was used. It had a 200 W pulse wave fiber laser with a focal diameter of 70 µm and a build volume of 250x250x300 mm. Spherical Inconel 718 powder, with particle size between 15 and 45 µm was used with chemical composition displayed in Table 1.

Element (w%)	**Al**	**C**	**Co**	**Cr**	**Cu**	**Fe**	**Mn**	**Mo**	**Ni**	**S**	**Si**	**Ti**
Renishaw powder (0405) [20]	0.2 to 0.8	0.02 to 0.05	<1.0	17.0 to 21.0	<0.3	Balance	<0.35	2.8 to 3.3	50.0 to 55.0	<0.015	<0.35	0.65to 1.15

Table 1: Composition of IN718 powder in wt %

Meander scanning was used for the volume fill of each layer as depicted in Figure 1 (a). With each layer, the volume was scanned first, followed by the internal and outer borders. The inner and outer borders were offset by the border distance and the laser scan paths. The laser spot scans each layer at an angle of 67o with respect to the previous one [47]. The process parameters used for the laser scanning are displayed in Table 2. Common process parameters that were used for the fill and border scan were the laser power set to 200 W, layer height at 30 mm, hatch spacing at 90 mm, and beam compensation at 60 mm. These AM process parameters for this alloy have been shown to be the optimum combination that delivers minimal porosity and defects to maximise the integrity of 3D printed thin-walled sections [31] .

	Units	**Fill hatch**	**Outer Border**	**Inner Border**
Laser power	W	200	200	200
Exposure time	µs	70	50	70
Point distance	µm	70	20	70
Scan speed	mm/s	1000	400	1000
Energy density	J/mm^3	74.1	185	74.1

Table 2: LPBF Process parameters used for tensile test samples

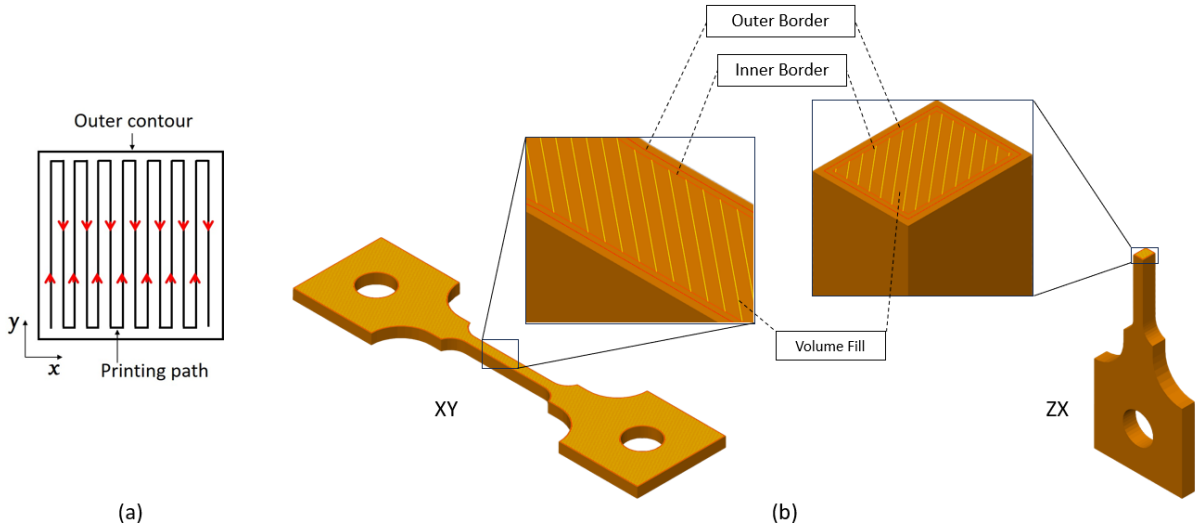

Figure 1: (a) Schematic of the meander strategy with the outer contour and the printing path using for the printed thin strut; (b) The scanning paths in the XY and ZX samples

Tensile test samples with dimensions as shown in Figure 2(a) were designed and additively manufactured in 2 building directions (BD), XY and ZX, as shown in Figure 2(b), to investigate their effects on microstructure as function of the process parameters. The scanning paths for each sample are shown in Figure 1 (b). Following the L-PBF process, the samples, still attached to the build plate, were stress relieved at a temperature of 982 °C for one hour, followed by slow cooling to room temperature within the furnace. Subsequently, the samples were separated from the substrate plate using a wire cut electrical discharge machining process (AgieCharmilles Cut E350). The wire diameter used ranged from 0.1 mm to 0.3 mm, and the axis speed varied from 0 to 3000 mm/min. This machining process was employed to minimize internal stress during sample removal.

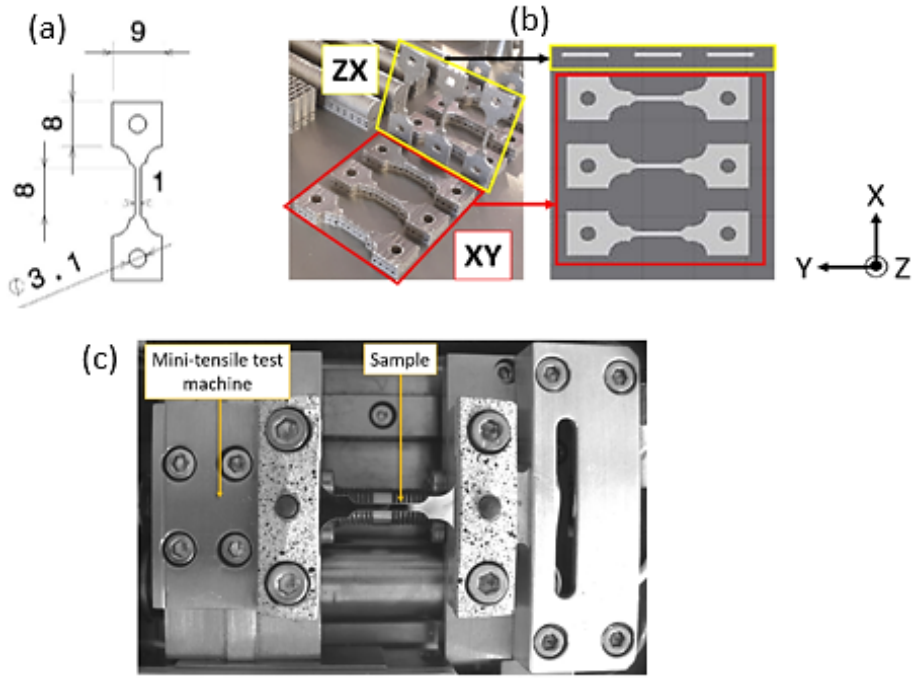

Figure 2: (a) tensile sample form and dimension in mm with a tolerance ±0.1 mm (b) Specimen printed in XY and ZX building direction on the substrate plate (pictures and CAD model) (c) specimen mounted in the micro-tensile machine

Microstructure characterization

For microstructural characterizations, the samples were polished with 9 µm, 3 µm and 1 µm diamond pasted, followed by chemo-mechanical polishing with colloidal silica suspension (OPS). SEM observations, Energy Dispersion Spectroscopy EDS analysis (for phase chemical composition determination) and EBSD measurement (for grain orientation determination) were performed using a ZEISS Supra 40 SEM, operating at 20 kV. EBSD measurements were made before and after deformation for each sample in the same zone, in the entire width of the sample which provided a map of 1450 µm x 1050 µm. The post-processing of the EBSD data was done with the ATEX software [48]. Enhanced BSE was carried out with a Zeiss Auriga SEM (Oberkochen, Germany) operating at 10 kV. Enhanced BSE enables to contrast grain disorientations, phases (Z-contrast) and even crystalline defects (dislocations, stacking faults) on a bulk sample [49-51].

Micro-Tensile Testing

To examine the microstructure evolution under uniaxial tensile loading, micro-tensile testing was conducted at room temperature using a DEBEN machine from Suffolk, UK. The machine was equipped with a maximum load cell capacity of 1 kN, as depicted in Figure 2c. During the testing, the samples were subjected to a strain rate of 4.10-4 s-1. The residual plastic strain after removing the load was 0.77%.

3.0 RESULTS

Initial Microstructures

Figure 3 (a) shows the section of the tensile test samples being analysed and Figures 3 (b) and (c) show the of the inverse pole figures (IPF) for ZX and XY samples, respectively. In both cases, distinct zones were symmetrically observed from the border to the center of each sample, with a finer microstructure in close proximity to the edges. The finer zones, denoted as zones 1 and 5, covered approximately 5 to 9% of the width. Subsequently, a transition zone was observed, characterized by larger columnar grains, which accounted for approximately 14 to 16.6% of the width. Finally, zone 3 represented the largest region of the specimen and exhibited columnar and equiaxed grain structures for the ZX and XY samples, respectively. It was also observed that [101] texture component was strongest in zone 3 for both XY and ZX.

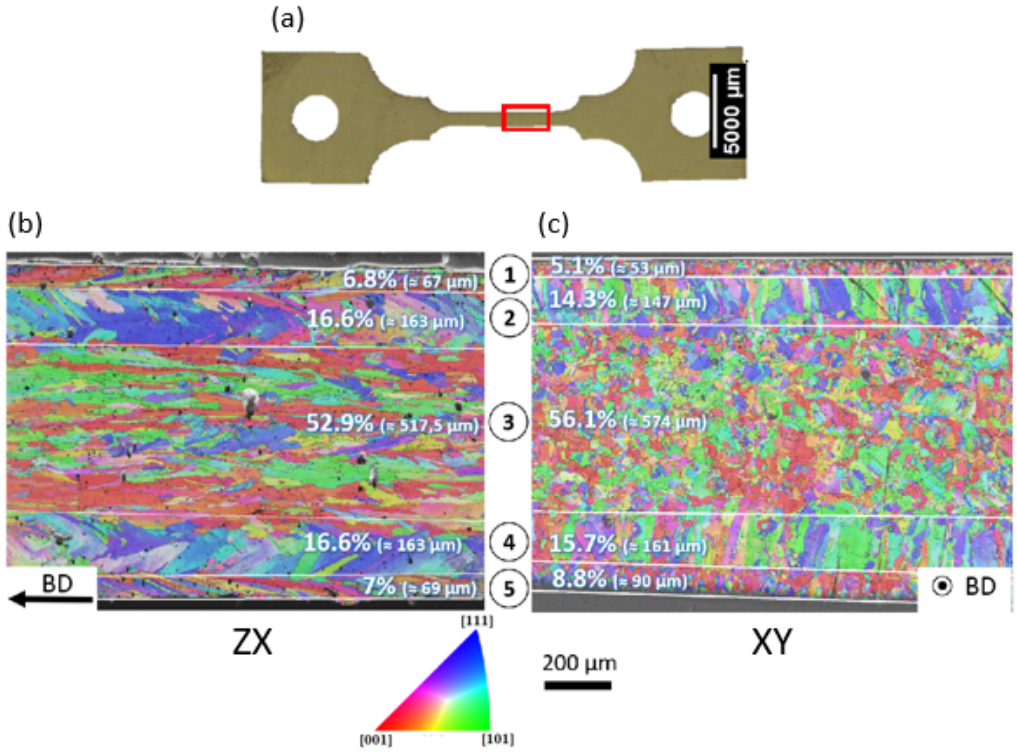

Figure 3: Inverse Pole Figure of ZX and XY building directions samples before load application

Figure 4 (a) displays a BSE micrograph of the specimen built in the XY build direction, exhibiting an equiaxed grain structure. On the other hand, Figure 4 (b) corresponds to the specimen built in the ZX build direction. Both BSE micrographs were captured from different specimens, specifically from the middle region of each sample. The BSE micrograph utilizes Z-contrast to highlight chemical elements with a higher atomic number, appearing as white compared to the matrix. Two distinct types of precipitates can be identified, characterized by globular and needle plate morphologies, indicated by dotted yellow and full red circles, respectively.

The characterization of both the precipitates and the matrix γ phase was performed using Energy Dispersion Spectroscopy (EDS), and the results are presented in Table 3. Local chemical analyses were conducted on the matrix as well as multiple precipitates to obtain average chemical compositions. The chemical composition of the matrix align with the provided chemical composition by the supplier. Both types of precipitates exhibit an enrichment of Nb and a depletion of Fe and Cr compared to the matrix γ phase, as shown in Table 3. Based on their chemical compositions, the globular precipitates are identified as Laves phase, while the needle-shaped precipitates correspond to the δ-phase [8] [12].

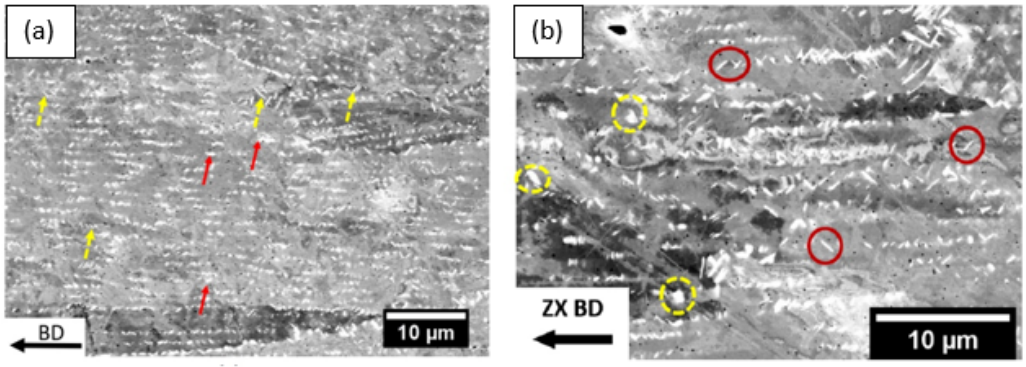

Figure 4: BSE microphotographs for (a) XY plane (b) ZX plane with precipitates looks like island in interdentritic region showed by dotted circle (Laves phase), and needle plate morphology showed by full circles (δ-phase)

	Ni	Cr	Fe	Nb	Ti	Al
Laves phase (globular shape)	57.7	11.9	11.6	15.6	1.7	0.3
δ-phase (needle shape)	52.8	16.8	16.2	9.2	1.3	0.4
Matrix γ	53.5	19.1	18.8	4.7	1	0.5

Table 3: Chemical composition (in wt%) on precipitates and matrix of printed Inconel 718

Microstructure after Deformation

Figure 5 illustrates the microstructure of the specimen built in the XY and ZX building direction, both before and after deformation. No significant changes in grain size and precipitates are observed in the micrographs of the XY samples as shown in Figure 5 (a and b).

For the ZX sample, a focused area with a uniform contrast, revealing the presence of precipitates in the interdentritic region (Laves phase), as indicated by the red circle (Figure 5 (c)) was compared before and after loading in Figure 5 (c) and (d) respectively. Note that the red circles are guides for the eyes to localize the region before and after deformation. In Figure 5 (d), a darker area is observed compared to the neighboring grain directly above it, as indicated by the black arrow. This contrast change signifies a misorientation in the observed area relative to the enhanced BSE micrograph.

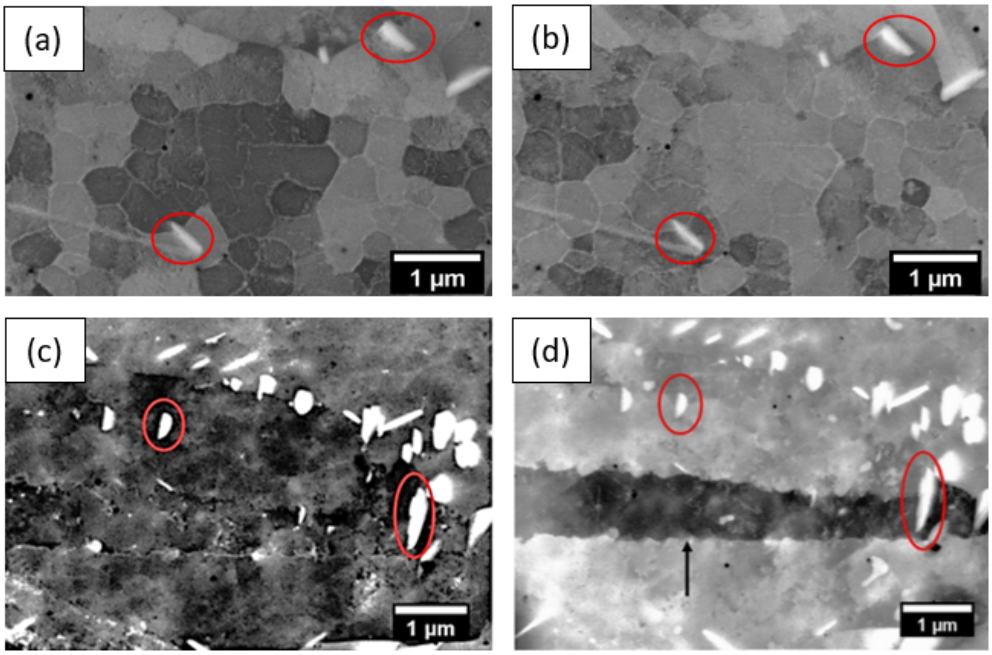

Figure 5: BSE micrographs of XY (a, b) and ZX (c, d) samples before and after deformation respectively.

Figure *6* presents EBSD orientation maps for both building directions (XY and ZX) before and after plastic deformation. Several zones are highlighted with black ellipses to identify the deformed grains following the uniaxial tensile testing. These orientation maps provide valuable information about the crystallographic orientation of the grains in the microstructure. By comparing the maps before and after plastic deformation, the changes in grain orientation can be analyzed, and the deformed grains can be identified within the highlighted zones.

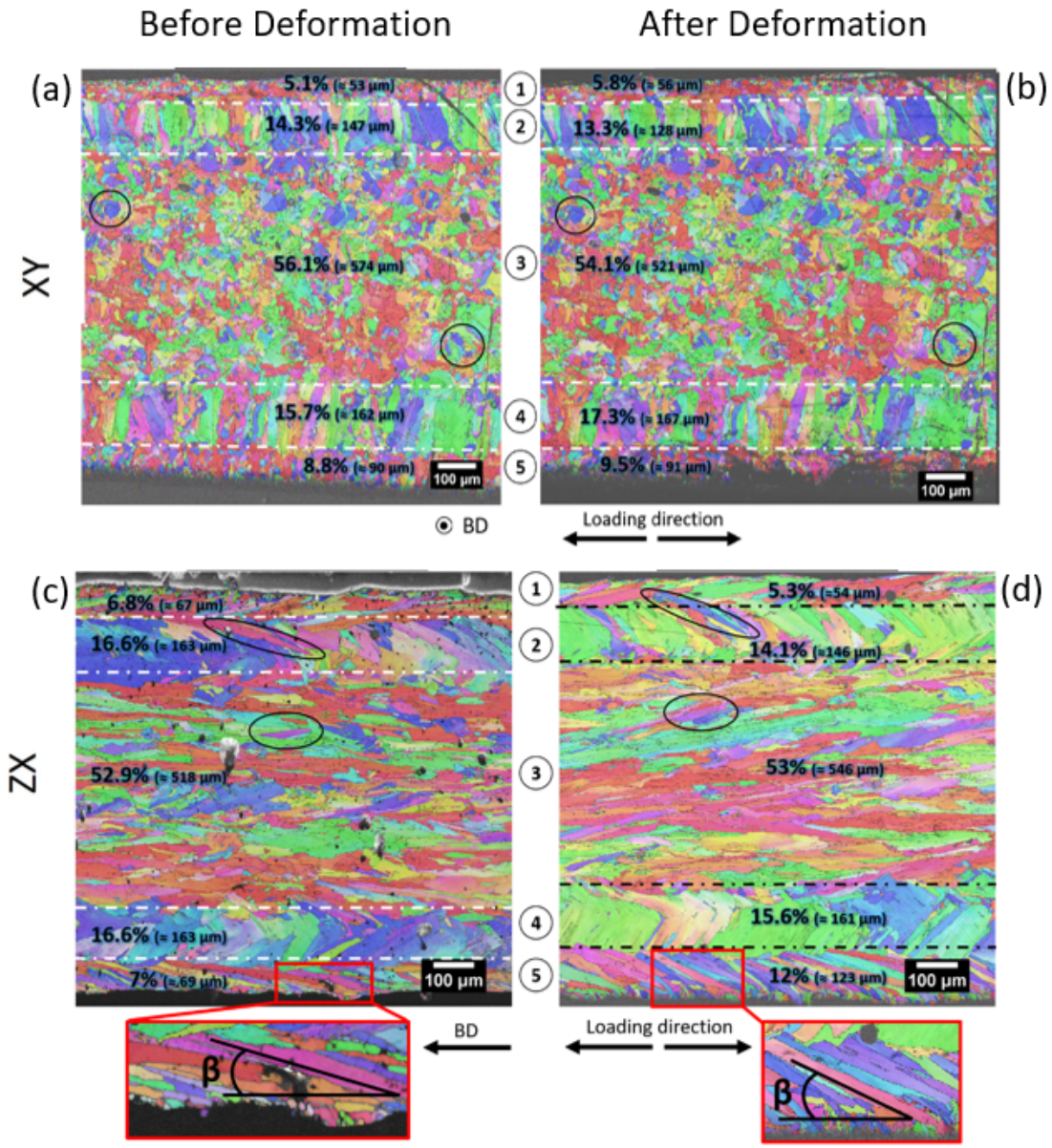

Figure 6: EBSD mapping of the XY (a and b) and ZX (c and d) samples, before and after deformation on the same area respectively

Figure 6 (a) and (b) shows the microstructure of XY before and after loading. No substantial difference in grain or area size and grain direction is observed. This suggests that the deformation process did not cause significant microstructural changes in the XY building direction.

In the case of the ZX building direction (Figure 6 (c and d)), there are noticeable differences between the two orientation maps, particularly in zones 3, 4, and 5, indicating significant changes in the microstructure after deformation. In zone 5, the size of the grains increases from 69 µm to 124 µm after deformation. Additionally, there is a rotation of the elongated grain within this zone, as depicted in the magnified micrograph in Figure 6(c and d). The angle β, which represents the angle between the growth direction of the elongated grain and the building direction, evolves from 15° to 25° (±4.7°) following deformation. Zone 4 exhibits larger grain sizes compared to the pre-deformation microstructure, indicating grain growth during the deformation process. On the other hand, in zone 3, the grains appear more elongated along the loading direction after deformation.

These observations suggest that the deformation process in ZX leads to distinct changes in grain size and shape, as well as grain rotation, within different zones of the microstructure.

The lateral deformation of the sample was quantified by measuring the width of the specimen before and after plastic deformation using ten measurements along the entire width of the sample. The initial width of the specimen was 0.98 mm, which increased to 1.05 mm after deformation, with a standard deviation of ± 0.02 mm. This indicates that the sample experienced a lateral expansion during the deformation process.

To analyze the grain size evolution, charts were plotted for each area before and after deformation using the ATEX software. It was observed that the microstructure does not exhibit a standard normal distribution in terms of grain size, indicating a heterogeneous microstructure. The main focus was on zones 3, 4, and 5, and the corresponding charts for these regions are shown in Figure 7.

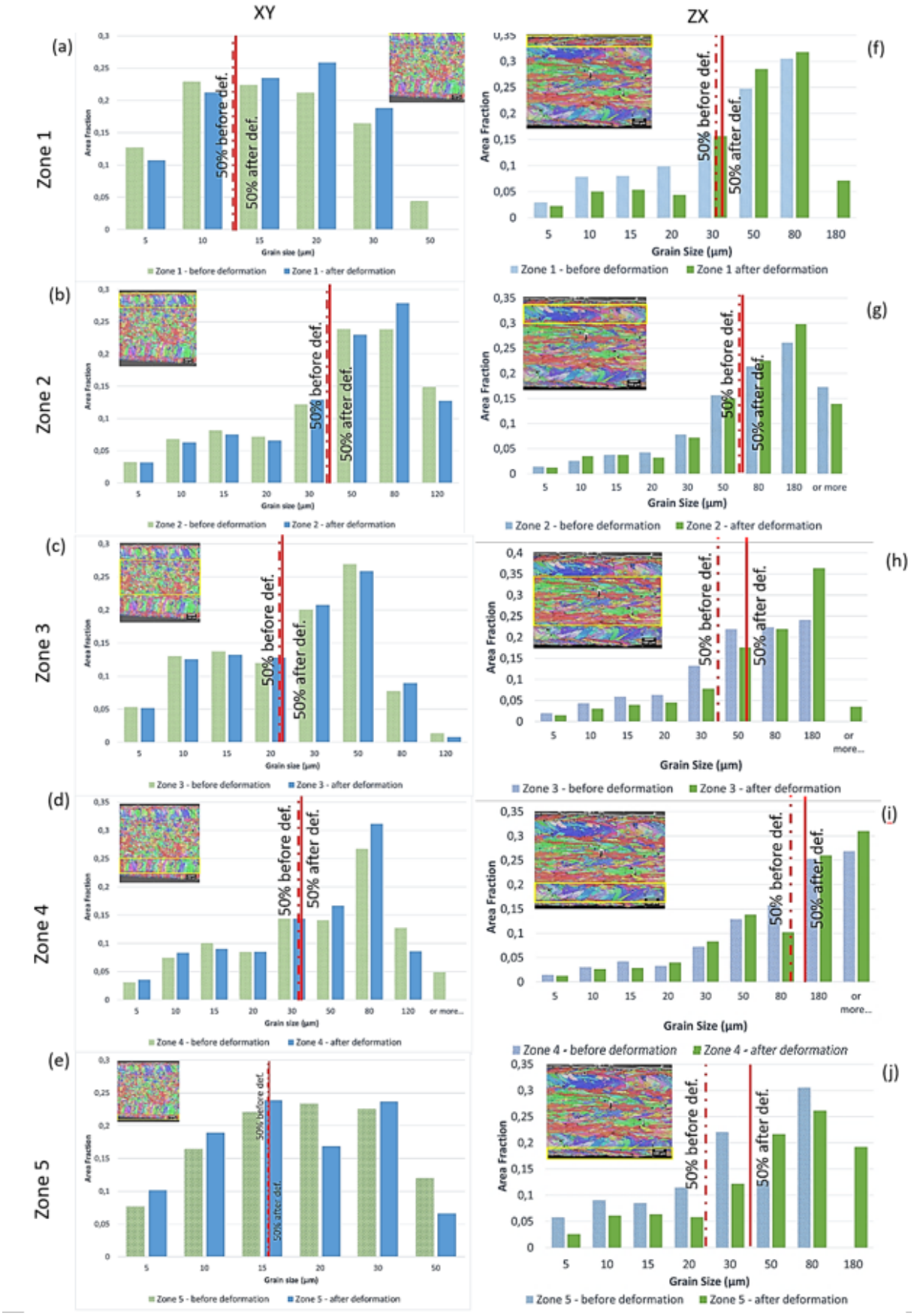

Figure 7: Grain size (µm) distribution with respect to area fraction for Zone 1, 2, 3, 4 and 5 for XY (a, b, c, d, e) and ZX (f, g, h, I, j) respectively.

The charts display the median grain size as a function of the area fraction, with the dotted red line representing the median before deformation and the solid red line representing the median

after deformation. It can be observed that, in general, the grain size increases after deformation in zones 3, 4, and 5, as shown in Figure 7. There was no major change in grain size distribution in zones 3, 4 and 5 for XY as shown in Figure 7 (a), (b) and (c) respectively. Conversely, significant changes in grain size distribution were observed for ZX sample as follows:

i. In zone 3, the fraction of grains with sizes ≤ 50 μm decreased, while the fraction of larger grains (≥ 180 μm) increased.
ii. In zones 2 and 4, the distribution of grain sizes remained relatively unchanged.
iii. In zones 1 and 5, the fraction of small grains (≤ 30 μm) decreased, while the fraction of larger grains (≥ 180 μm) increased.

These findings suggest that the plastic deformation process resulted in an increase in grain size, particularly in zones 3, 4, and 5, while the distribution of grain sizes in other zones remained relatively unaffected.

4.0 DISCUSSION

Effect of Build Direction on IN718 Microstructure

The samples printed in the XY build direction exhibit equiaxed grains, while those printed in the ZX direction have elongated and columnar grains parallel to the building axis as shown in Figure 3. This difference in microstructural architecture is characteristic of the laser powder bed fusion (L-PBF) process, which involves complex heat flux dynamics. For the ZX samples, the laser provides a heat source that interacts with the powder layer, resulting in heat transfer between the previously deposited layer and the current substrate [52, 53]. The remelted zone under the laser forms a new interface between these layers, leading to metallurgical bonding [52]. Instead of nucleating new grains, the grains grow epitaxially along the preferential growth direction, which is theoretically perpendicular to the melt pool due to the maximum heat flux. However, the Marangoni convection, driven by heat-mass transfer effects, can deviate the heat flux and cause the growth direction to have a slight angle from the building direction, as observed in Figure 3. For the XY samples, the temperature between different meltpools is somewhat similar resulting in a low thermal gradient G in the volume region. Together with a high cooling rate, and thus high grain growth R, the low G results in a low solidification rate G/R and thus grains with similar dimensions are formed in all directions.

The results (Figure 4 and Table 3) indicate that the microstructure of Inconel 718 produced by powder bed fusion consists of two types of precipitates, with an enrichment in Nb for both types. The globular precipitates, which exhibit a higher content of Nb (average of 15.6% wt), are identified as Laves phase, as supported by previous studies [12, 13]. The precipitates with a needle and plate morphologies, on the other hand, are identified as δ-phase, consistent with the findings of Azadian et al. [8]. The formation of δ-phase is typically associated with prolonged thermal treatments between 700°C and 1000°C [15]. Interestingly, these temperature ranges are similar to those reached during the L-PBF process for the fusion of Inconel 718 powder. The EDS measurements of the main matrix γ showed a Nb content of about 5% wt, which is the minimum required amount of Nb for δ-phase formation [12]. For the formation of Laves phase, a Nb content between 10% and 12% wt, along with temperatures ranging from 650°C to 1000°C, is required [11, 12]. These temperature ranges correspond to the temperatures within the melting pool during the L-PBF process. Based on the comparison of Nb quantities in the two phases, it can be inferred that Laves phase forms after the δ-phase, predominantly precipitating in the interdentritic region. Furthermore, the stress-relieving heat treatment reduces the amount of Laves phase by homogenizing the microstructure, which explains the lower quantity of Laves phase precipitates observed in the samples compared to δ-phase.

The quantity and distribution of precipitates vary depending on the build direction. On the XY plane, where the microstructure consists of equiaxed grains, the precipitates are mainly concentrated along the grain boundaries (Figure 5 (a)). The rapid solidification in the XY

direction also limits the time available for precipitates to nucleate resulting in a lower precipitate density in the XY build direction. In contrast, the ZX plane, which exhibits a dendritic structure with columnar grains developed through the heat flux and layer-by-layer process, shows precipitates both along the grain boundaries and in the interdentritic region (Figure 5b). This difference can be attributed to the specific microstructure of each building direction. In the case of the ZX building direction, microsegregation occurs in the interdentritic region, leading to the formation of Laves phase with Nb enrichment [11]. Delta-phase can also be observed within the grains, caused by the microsegregation of Nb induced by the rapid cooling of Inconel 718 during the process, as reported by Trosch et al. [14].

Complex Microstructure of LPBF IN718 thin struts

Figure 6 shows varying microstructure in the printed Inconel 718 samples, where the microstructure varies from the edge to the middle bulk of the sample. Similar observations have been made by Tang et al. [54] for nickel based superalloys ABD 850 AM, CM247LC and IN939 cubes (10 mm by 10 mm by 10 mm) manufactured by a LPBF process. The researchers also used a meander scanning strategy for the AM process whereby the border scanning was associated with the local grain growth at the edges of the cube samples. Langi et al. [41] also observed a similar complex microstructure in stainless steel 316L cylindrical samples (8 mm diameter and 0.5 mm wall thickness), and Jhabvala et al. [40] reported it in gold cube samples (5mm by 5mm by 5mm), both manufactured using L-PBF. Yang et al. [42] also found different microstructures in thin walls of varying scanning speeds in Inconel 718.

In the ZX building direction, zones 1 and 5 showed columnar grains with a grain growth direction forming an angle with the building direction. The transition zones, zones 2 and 4, exhibited larger grains, while the most significant zone was the third one, with elongated grains along the building direction. The variation in grain morphology is primarily attributed to the heat flux and rapid cooling during the additive manufacturing process. According to the model proposed by Hunt [54] and studied by Gaumann et al. [52], the development of equiaxed and columnar grains is influenced by the temperature gradient (G) and the growth rate (R). The product of G and R, representing the cooling rate, determines the final microstructure. A low value of G x R leads to columnar microstructure, while a high value results in equiaxed grains [55]. Additionally, a higher solidification rate (G/R) contributes to a finer columnar structure [41]. Therefore, the thermal gradient and growth rate are fundamental factors for predicting the microstructure in terms of columnar or equiaxed dendrites.

The microstructure change at the edge is explained by the thermal gradient during the L-PBF process and the scanning strategy employed. The meander scanning strategy involves filling the volume with parallel paths along two opposite directions, followed by melting the outer contour of the specimen. As a result, the powder in the volume is the first to be melted, creating a melting pool and allowing grain growth along the liquid/solid interface determined by the laser energy density [55, 56] and building direction [5, 33]. Subsequently, the outer contour is traced by the laser, creating a high thermal gradient between the border zone, the volume, and the unmelted powder. This high cooling rate near the edge leads to a finer microstructure in the border zone. This has also been associated with the remelting process during the border scanning after the volume scan [57].

Meanwhile, the volume (zone 3) starts cooling down before the border zone. The thermal gradient between the border and the volume (zones 1 or 5 and zone 3) results in different solidification and cooling rates, causing the microstructure to evolve and form a transition zone joining the two zones. Hunt et al. [59] described the existence of a Columnar Equiaxed Transition (CET), which depends on the thermal gradient (G), solid/liquid interface velocity (R), and the number of nucleants. Depending on the thermal gradient and growth rate, the grain morphology can be either finer and equiaxed or columnar. However, for certain values of G and R, a transition from columnar to equiaxed grains can occur (as seen in the XY samples for

zone 2 and 4), leading to the formation of a complex microstructure known as the transition zone.

Raghavan et al. [60] conducted a numerical study on the heat transfer and grain morphology of Inconel 718 printed using Electron Beam Melting. Their results demonstrated that the microstructure depends on various process parameters, which influence grain morphology and the CET during solidification of the melting pool. A high solidification rate (i.e., high G and low R) at the beginning leads to columnar grains, while the end of solidification results in equiaxed grains. The transition zone observed in the samples can be seen as a CET zone with different microstructure, thus creating a microstructure gradient. In the XY build direction, elongated grains were present in Zone 2 and 4, as compared to the equiaxed grains in zone 1, 3 and 5. This was associated with the high volume energy density (VED) outer border scan happening after the low VED inner border. The high thermal gradient created between inner and outer border scans caused the molten pool to extend horizontally across the build direction resulting in directional solidification along XY in Zone 2 and 4.

The microstructure change observed in the printed Inconel 718 samples is a result of the thermal gradient and cooling rates during the L-PBF process. The scanning strategy and the interaction between the border zone, volume, and unmelted powder contribute to the formation of different microstructures. The thermal gradient, growth rate, and CET play crucial roles in determining whether the grains are columnar or equiaxed, and the transition zone represents a complex microstructure between the two. Considering the tensile test samples gauge width and that less than 50% of the latter width (44% for XY and 47% for ZX) have different microstructure than the bulk; it was assumed that the mechanical properties of the thin wall structures such as a strut will be influenced by the LPBF printing parameters and scanning strategy. In samples with larger width, the edge effect is minimal considering the ratio of the different grains is minimal [61].

Microstructure Change under loading at low plastic strain

Under tensile loading, the microstructure of the samples printed in the XY building direction did not exhibit significant changes in terms of microstructure gradient and grain size as shown in Figure 5, 6 and 8. The loading on the XY samples occurs perpendicular to the grain direction and against more grain boundaries with strengthening precipitates as shown in Figure 3 and 4. However, the samples printed in the ZX build direction showed a distinct evolution of the microstructure.

One noticeable change was observed in zone 5, which increased in width from 69 μm to 124 μm after deformation in the ZX building direction. In Figures 6 (c and d) and 7 (j), it can be observed that the grains became larger and more elongated after deformation. Additionally, the grains appeared to rotate from the volume towards the border, as depicted in Figure 4 (a). Since zone 5 is adjacent to zone 4, where the movement of grains required high energy, the grains in zone 5 were able to rearrange and grow while rotating. This rotation of grains applied a force on the border, leading to lateral expansion of the sample. Rotational deformation has been observed in nanocrystalline ceramics and metals as a result of non-equilibrium grain boundaries. In order to achieve an equilibrium solution, an unconstrained grain may rotate to lower its energy and adjust the misorientation of the two boundaries. It can be assumed that the grains rotated at their respective boundaries during deformation. Rotational deformation is a novel aspect in the context of polycrystals. However, this particular microstructural evolution was specific to the ZX build direction and was not observed in the XY build direction. The combination of columnar microstructure at the edge and the microstructure gradient is necessary to provide a negative Poisson's ratio under tensile load.

Another change in the microstructure was observed in zone 4 of the ZX samples. The grain size increased after deformation, which can be associated with a phenomenon called Stress Induced

Boundary Migration (SIBM) driven by Energy Density Jump (EDJ). During loading, in the presence of defects such as porosity in the microstructure (which is the case for the studied material), the grains tend to reduce their total energy through boundary migration. The migration direction depends on the surface energy, occurring from the side with lower surface energy to the side with higher surface energy. If the equilibrium state is not reached, additional grain rotation can occur to adjust the local misorientations.

In summary, the reorganization of the microstructure under tensile loading in the ZX build direction samples is facilitated by grain boundary migration coupled with rotational deformation. The grain size increases, and the grains tend to rotate to achieve an equilibrium state within the microstructure at the microscale under tensile loading.

5.0 CONCLUSION

This paper investigated the microstructure of Inconel 718 produced by L-PBF and examined its evolution under plastic deformation through uniaxial micro-tensile testing. The following key findings were observed:

i. The presence of Laves phase and δ-phase on interdendritic and grain boundaries regions was attributed to the temperature range of the melting pool and the amount of Nb present in Inconel 718. The BSE micrographs suggested that the XY building direction contained fewer precipitates compared to ZX which was linked to the rapid solidification process .
ii. A variation in microstructure was observed, divided into three zones symmetrically from the border to the center. This variation was a characteristic feature of the L-PBF process and was influenced by the thermal gradient and solidification rate associated with the border scan during a meander scanning strategy.
iii. Both the XY and ZX building directions exhibited variation in microstructure in the same manner, but with different grain sizes and shapes. Both XY and ZX, exhibited fine columnar grains in the zone 2 and 4 [Inner border of sample]. The presence of columnar grains in the XY samples was attributed to the high thermal gradient between inner and outer border scan. ZX displayed columnar grains, while XY exhibited equiaxed grains in the main volume and outer borders of the sample.
iv. No significant change in struts microstructure was observed in XY sample after tensile loading.
v. A distinct evolution of the microstructure was observed in ZX under loading. The non-equilibrium state of the columnar grain shape and grain size distribution led to rotational deformation and grain boundary migration, resulting in the attainment of an equilibrium state within the microstructure.

Overall, this study provided valuable insights into the microstructural characteristics and evolution of Inconel 718 produced by L-PBF. The findings contribute to a better understanding of the relationship between process parameters, microstructure, and mechanical properties, which can aid in the optimization of L-PBF processes for Inconel 718 and similar materials.

ACKNOWLEDGEMENTS

This research was sponsored by the French Ministry of Education in France and University of Derby's College of Science and Engineering (CoSE) in England. The research was carried out at LEM3 of the University of Lorraine in Metz and the Institute for Innovation within CoSE. The PhD supervisors were Prof. Alexis Rusinek and Prof. Paul Wood, supported by Dr Urvashi Gunputh and Dr Slim Bahi. The wider supervisory team are stated in the list of coauthors.

REFERENCES

1. Çam, G. and M. Koçak, *Progress in joining of advanced materials.* International Materials Reviews, 1998. **43**(1): p. 1-44.
2. Le Coz, G., *Usinage de l'INCONEL 718 : Intégrité de surface, mesure de température et modèle analytique du fraisage périphérique*. 2013.
3. Liu, F., et al., *The effect of laser scanning path on microstructures and mechanical properties of laser solid formed nickel-base superalloy Inconel 718.* Journal of Alloys and Compounds, 2011. **509**(13): p. 4505-4509.
4. Deng, D., et al., *Microstructure and mechanical properties of Inconel 718 produced by selective laser melting: Sample orientation dependence and effects of post heat treatments.* Materials Science and Engineering: A, 2018. **713**: p. 294-306.
5. Amato, K.N., et al., *Microstructures and mechanical behavior of Inconel 718 fabricated by selective laser melting.* Acta Materialia, 2012. **60**(5): p. 2229-2239.
6. Tucho, W.M., et al., *Microstructure and hardness studies of Inconel 718 manufactured by selective laser melting before and after solution heat treatment.* Materials Science and Engineering: A, 2017. **689**: p. 220-232.
7. Anderson, M., et al., *δ Phase precipitation in Inconel 718 and associated mechanical properties.* Materials Science and Engineering: A, 2017. **679**: p. 48-55.
8. Azadian, S., L.-Y. Wei, and R. Warren, *Delta phase precipitation in Inconel 718.* Materials Characterization, 2004. **53**(1): p. 7-16.
9. Li, R.B., et al., *Isolation and determination for δ, γ′ and γ″ phases in Inconel 718 alloy.* Scripta Materialia, 2002. **46**(9): p. 635-638.
10. Shi, J.J., et al., *Study on the microstructure and creep behavior of Inconel 718 superalloy fabricated by selective laser melting.* Materials Science and Engineering: A, 2019. **765**: p. 138282.
11. Radhakrishna, C.H. and K. Prasad Rao, *The formation and control of Laves phase in superalloy 718 welds.* Journal of Materials Science, 1997. **32**(8): p. 1977-1984.
12. Radavich, J.F., *The Physical Metallurgy of Cast and Wrought Alloy 718*. 2004. 229-240.
13. Zhang, Y., et al., *Effect of Heat Treatment on Niobium Segregation of Laser-Cladded IN718 Alloy Coating.* Metallurgical and Materials Transactions A, 2013. **44**(2): p. 708-716.
14. Trosch, T., et al., *Microstructure and mechanical properties of selective laser melted Inconel 718 compared to forging and casting.* Materials Letters, 2016. **164**: p. 428-431.
15. Verma, A., et al., *Evolution of Delta Phase Microstructure in Alloy 718*. 2010. 737-750.
16. Parimi, L.L., et al., *Microstructural and texture development in direct laser fabricated IN718.* Materials Characterization, 2014. **89**: p. 102-111.
17. Sjöberg, G., N.G. Ingesten, and R.G. Carlson, *Grain Boundary δ-Phase Morphologies, Carbides and Notch Rupture Sensitivity of Cast Alloy 718.* Superalloys, 1991: p. 603-620.
18. Chlebus, E., et al., *Effect of heat treatment on the microstructure and mechanical properties of Inconel 718 processed by selective laser melting.* Materials Science and Engineering: A, 2015. **639**: p. 647-655.
19. Wang, X. and K. Chou, *The effects of stress relieving heat treatment on the microstructure and residual stress of Inconel 718 fabricated by laser metal powder bed fusion additive manufacturing process.* Journal of Manufacturing Processes, 2019. **48**: p. 154-163.
20. Sienkiewicz, J., et al., *Investigations on the Mechanical Response of Gradient Lattice Structures Manufactured via SLM.* Metals, 2020. **10**(2): p. 213.
21. Xiong, J., et al., *Structural optimization of re-entrant negative Poisson's ratio structure fabricated by selective laser melting.* Materials & Design, 2017. **120**: p. 307-316.

22. Jia, Q. and D. Gu, *Selective laser melting additive manufacturing of Inconel 718 superalloy parts: Densification, microstructure and properties.* Journal of Alloys and Compounds, 2014. **585**: p. 713-721.
23. Moussaoui, K., et al., *Effects of Selective Laser Melting additive manufacturing parameters of Inconel 718 on porosity, microstructure and mechanical properties.* Materials Science and Engineering: A, 2018. **735**: p. 182-190.
24. Ghouse, S., et al., *The influence of laser parameters and scanning strategies on the mechanical properties of a stochastic porous material.* Materials & Design, 2017. **131**: p. 498-508.
25. Yi, J.H., et al., *Effect of laser energy density on the microstructure, mechanical properties, and deformation of Inconel 718 samples fabricated by selective laser melting.* Journal of Alloys and Compounds, 2019. **786**: p. 481-488.
26. Carter, L.N., et al., *The influence of the laser scan strategy on grain structure and cracking behaviour in SLM powder-bed fabricated nickel superalloy.* Journal of Alloys and Compounds, 2014. **615**: p. 338-347.
27. Cheng, B., S. Shrestha, and K. Chou, *Stress and deformation evaluations of scanning strategy effect in selective laser melting.* Additive Manufacturing, 2016. **12**: p. 240-251.
28. Rashid, R., et al., *Effect of scan strategy on density and metallurgical properties of 17-4PH parts printed by Selective Laser Melting (SLM).* Journal of Materials Processing Technology, 2017. **249**: p. 502-511.
29. Choi, J.-P., et al., *Densification and microstructural investigation of Inconel 718 parts fabricated by selective laser melting.* Powder Technology, 2017. **310**: p. 60-66.
30. Sufiiarov, V.S., et al., *The Effect of Layer Thickness at Selective Laser Melting.* Procedia Engineering, 2017. **174**: p. 126-134.
31. Wood, P., et al., *High strain rate effect on tensile ductility and fracture of AM fabricated Inconel 718 with voided microstructures.* Materials & Design, 2021. **208**: p. 109908.
32. Wang, X., T. Keya, and K. Chou, *Build Height Effect on the Inconel 718 Parts Fabricated by Selective Laser Melting.* Procedia Manufacturing, 2016. **5**: p. 1006-1017.
33. Sun, S.-H., et al., *Electron beam additive manufacturing of Inconel 718 alloy rods: Impact of build direction on microstructure and high-temperature tensile properties.* Additive Manufacturing, 2018. **23**: p. 457-470.
34. Vilaro, T., et al., *Microstructural and mechanical approaches of the selective laser melting process applied to a nickel-base superalloy.* Materials Science and Engineering: A, 2012. **534**: p. 446-451.
35. Wang, X. and K. Chou, *Electron Backscatter Diffraction Analysis of Inconel 718 Parts Fabricated by Selective Laser Melting Additive Manufacturing.* JOM, 2017. **69**(2): p. 402-408.
36. Wauthle, R., et al., *Effects of build orientation and heat treatment on the microstructure and mechanical properties of selective laser melted Ti6Al4V lattice structures.* Additive Manufacturing, 2015. **5**: p. 77-84.
37. Delcuse, L., et al., *Effect of powder bed fusion laser melting process parameters, build orientation and strut thickness on porosity, accuracy and tensile properties of an auxetic structure in IN718 alloy.* Additive Manufacturing, 2020. **36**: p. 101339.
38. Jia, H., et al., *Scanning strategy in selective laser melting (SLM): a review.* The International Journal of Advanced Manufacturing Technology, 2021. **113**(9): p. 2413-2435.
39. Tian, Y., et al., *Influences of processing parameters on surface roughness of Hastelloy X produced by selective laser melting.* Additive Manufacturing, 2017. **13**: p. 103-112.
40. Jhabvala, J., E. Boillat, and R. Glardon, *On the use of EBSD analysis to investigate the microstructure of gold samples built by selective laser melting.* Gold Bulletin, 2011. **44**(2): p. 113-118.

41. Langi, E., et al., *Microstructural and Mechanical Characterization of Thin-Walled Tube Manufactured with Selective Laser Melting for Stent Application.* Journal of Materials Engineering and Performance, 2021. **30**(1): p. 696-710.
42. Yang, H., et al., *The printability, microstructure, crystallographic features and microhardness of selective laser melted Inconel 718 thin wall.* Materials & Design, 2018. **156**: p. 407-418.
43. Venkatraman, K., et al., *Tuning critical resolved shear stress ratios for bcc-titanium Ti21S via an automated data analysis approach.* Modelling and Simulation in Materials Science and Engineering, 2021. **29**(5): p. 055014.
44. Ben Haj Slama, M., et al., *In Situ Macroscopic Tensile Testing in SEM and Electron Channeling Contrast Imaging: Pencil Glide Evidenced in a Bulk β-Ti21S Polycrystal.* Materials (Basel), 2019. **12**(15).
45. Xu, A., M. Saleh, and D. Bhattacharyya, *Experimental and computational analysis of the in situ tensile deformation of 2D honeycomb lattice structures in Ni single crystals.* Composites Part B: Engineering, 2020. **186**: p. 107823.
46. Ben Haj Slama, M., et al., *Electron channeling contrast imaging characterization and crystal plasticity modelling of dislocation activity in Ti21S BCC material.* Materialia, 2021. **15**: p. 100996.
47. Dario, P., et al., *Finite Element Thermal Analysis of Metal Parts Additively Manufactured via Selective Laser Melting*, in *Finite Element Method*, P. Răzvan, Editor. 2017, IntechOpen: Rijeka. p. Ch. 6.
48. Fundenberger, J.-J. and B. Beausir. *ATEX-Software*. 2017 [cited 2022; Available from: http://www.atex-software.eu/.
49. Kriaa, H., A. Guitton, and N. Maloufi, *Fundamental and experimental aspects of diffraction for characterizing dislocations by electron channeling contrast imaging in scanning electron microscope.* Scientific Reports, 2017. **7**(1): p. 9742.
50. Kriaa, H., A. Guitton, and N. Maloufi, *Modeling Dislocation Contrasts Obtained by Accurate-Electron Channeling Contrast Imaging for Characterizing Deformation Mechanisms in Bulk Materials.* Materials (Basel), 2019. **12**(10).
51. Kriaa, H., A. Guitton, and N. Maloufi, *Modelling Electron Channeling Contrast Intensity of Stacking Fault and Twin Boundary Using Crystal Thickness Effect.* Materials (Basel), 2021. **14**(7).
52. Gäumann, M., et al., *Epitaxial laser metal forming: analysis of microstructure formation.* Materials Science and Engineering: A, 1999. **271**(1): p. 232-241.
53. Gäumann, M., et al., *Single-crystal laser deposition of superalloys: processing–microstructure maps.* Acta Materialia, 2001. **49**(6): p. 1051-1062.
54. Tang, T., et al., *Alloys-By-Design: Application to New Superalloys for Additive Manufacturing.* Acta Materialia, 2020. **202**.
55. Gan, J., et al., *Effect of laser energy density on the evolution of Ni4Ti3 precipitate and property of NiTi shape memory alloys prepared by selective laser melting.* Journal of Alloys and Compounds, 2021. **869**: p. 159338.
56. Cui, X., et al., *Additive manufacturing of 24CrNiMo low alloy steel by selective laser melting: Influence of volumetric energy density on densification, microstructure and hardness.* Materials Science and Engineering: A, 2021. **809**: p. 140957.
57. AlMangour, B., D. Grzesiak, and J.-M. Yang, *Scanning strategies for texture and anisotropy tailoring during selective laser melting of TiC/316L stainless steel nanocomposites.* Journal of Alloys and Compounds, 2017. **728**: p. 424-435.
58. Watring, D.S., et al., *Effects of laser-energy density and build orientation on the structure-property relationships in as-built Inconel 718 manufactured by laser powder bed fusion.* Addit Manuf, 2020. **36**.
59. Hunt, J.D., *Steady state columnar and equiaxed growth of dendrites and eutectic.* Materials Science and Engineering, 1984. **65**(1): p. 75-83.

60. Raghavan, N., et al., *Numerical modeling of heat-transfer and the influence of process parameters on tailoring the grain morphology of IN718 in electron beam additive manufacturing.* Acta Materialia, 2016. **112**: p. 303-314.
61. PLEASS, C., *Powder Characterisation, Microstructure, and Mechanical Property Evolution of IN625 and IN718 During Selective Laser Melting and Heat Treatment*. 2021: Swansea.